Earth's Future

RESEARCH ARTICLE
10.1029/2021EF002272

Key Points:

- The pattern of rainfall change shows reversal asymmetry over the Indian Ocean during the radiative forcing (RF) increase and stabilization
- The pattern of rainfall response is determined by the coupling between dynamic circulation and sea surface temperature (SST)
- During the RF stabilization, ocean temperature change drives ocean heat transport leading to changes in SST

Supporting Information:

Supporting Information may be found in the online version of this article.

Correspondence to:

X. Qu and G. Huang,
quxia@mail.iap.ac.cn;
hg@mail.iap.ac.cn

Citation:

Hou, H., Qu, X., & Huang, G. (2021). Reversal asymmetry of rainfall change over the Indian Ocean during the radiative forcing increase and stabilization. *Earth's Future*, *9*, e2021EF002272. https://doi.org/10.1029/2021EF002272

Received 17 JUN 2021
Accepted 13 OCT 2021

Author Contributions:

Conceptualization: Xia Qu, Gang Huang
Data curation: Hongyu Hou
Formal analysis: Hongyu Hou, Xia Qu
Funding acquisition: Gang Huang
Investigation: Hongyu Hou
Methodology: Xia Qu, Gang Huang
Project Administration: Gang Huang
Software: Hongyu Hou
Supervision: Gang Huang

Reversal Asymmetry of Rainfall Change Over the Indian Ocean During the Radiative Forcing Increase and Stabilization

Hongyu Hou[1,4], Xia Qu[1,2], and Gang Huang[1,3,4]

[1]State Key Laboratory of Numerical Modeling for Atmospheric Sciences and Geophysical Fluid Dynamics, Institute of Atmospheric Physics, Chinese Academy of Sciences, Beijing, China, [2]Center for Monsoon System Research, Institute of Atmospheric Physics, Chinese Academy of Sciences, Beijing, China, [3]Laboratory for Regional Oceanography and Numerical Modeling, Qingdao National Laboratory for Marine Science and Technology, Qingdao, China, [4]University of Chinese Academy of Sciences, Beijing, China

Abstract The rainfall responses over the Indian Ocean (IO) are investigated based on the Representative Concentration Pathways 4.5 (RCP4.5) experiments of 13 models, in which the experiments are extended to the year 2300, from the Coupled Model Intercomparison Project Phase 5 (CMIP5). During the radiative forcing (RF) increase, the rainfall pattern displays northwest-southeast dipole asymmetry. After RF stabilization, rainfall increases over the southern IO and decreases over the northern IO where is a wet region in climatology. Diagnostic analysis demonstrates that both the changes in atmospheric circulation (dynamic component) and the moisture increase (thermodynamic component) play a key role in determining this rainfall dipole during RF increase, but the effect of the latter is reduced after RF stabilization. The responses of rainfall, sea surface temperature (SST) and atmospheric circulation are well coupled during the two periods: (a) the anomalous circulation affects the rainfall change by transporting abundant moisture to maintain the energy balance, with easterlies (northerlies) in RF increase (stabilization); and (b) in turn, heat released by the SST warming further induces the circulation change. Furthermore, during RF increase, the attribute of SST pattern is mainly led by ocean dynamics, especially heat transport due to ocean current changes, while after RF stabilization, it is mainly due to ocean heat transport leading by temperature changes.

Plain Language Summary Concentrations of greenhouse gases in the atmosphere have been increasing since the industrial revolution. However, the 2015 Paris Agreement proposed that we should pursue efforts to limit the global average temperature increase to 1.5°C above pre-industrial levels which requires the radiative forcing (RF) to decrease or stabilize. Due to the ocean thermal diffusion or other ocean dynamic processes, heat accumulated in upper layers persistently transmits downward to alter the oceanic stratification and furthermore, may influence the climatic responses. The present research focuses on the patterns of rainfall change over the Indian Ocean (IO) during RF increase and stabilization. When RF increases, the rainfall increases over the tropical northern IO but decreases over the southeastern IO; after RF stabilization, the rainfall over the IO displays a southwest-northeast dipole. This reversal asymmetry of rainfall change is determined by the coupling between dynamic circulation and sea surface temperature (SST), and the SST change is mainly due to the ocean heat transport driven by ocean temperature change after RF stabilization. These findings indicate that the deeper ocean warming plays an important role in climatic feedbacks after RF stabilization and we cannot ignore its effect.

1. Introduction

Since the industrial revolution, the concentrations of greenhouse gases in the atmosphere have been increasing as a result of human activities. The increase reduces the outgoing longwave radiation and stores more energy in the climate system, which has a direct influence on the global climate (Boer et al., 2000; von Schuckmann et al., 2016; Wang et al., 2020). Because of its large heat capacity, the ocean acts as heat storage, and approximately 93% of redundant energy is absorbed by the ocean, largely lowering the increase in the global mean surface temperature (Bryan et al., 1982; Hoffert et al., 1980; IPCC, 2018; Manabe & Stouffer, 2007; von Schuckmann et al., 2016). Heat absorption by the ocean generally begins at the surface,

Validation: Xia Qu
Visualization: Hongyu Hou, Xia Qu
Writing – original draft: Hongyu Hou
Writing – review & editing: Xia Qu

and there are significant warming signals in all ocean basins around the world during 1960–2019 (Cheng et al., 2020); then, it transmits energy downward by thermal diffusion or other ocean dynamic processes. The upper ocean warms faster than the deeper ocean during the radiative forcing (RF) increase, which previous studies have mainly focused on (Chadwick, Boutle, & Martin, 2013; Hwang et al., 2017; Ma et al., 2018; Qu et al., 2015; Xie et al., 2010).

However, the 2015 Paris Agreement proposed a target "Holding the increase in the global average temperature to well below 2°C above pre-industrial levels and pursuing efforts to limit the temperature increase to 1.5°C above pre-industrial levels." Realization of this target requires RF to decrease or stabilize (Sanderson et al., 2016). Little research has given attention to the climatic response to this RF scenario. After RF stabilization in the Representative Concentration Pathways 4.5 (RCP4.5) scenario, the warming rate of the deeper ocean is gradually greater than that of the upper ocean, and obvious warming occurs at 100–2,000 m; by 2250, the amplitudes of the total temperature increase in the upper 2,000 m are nearly uniform (Long, Liu, et al., 2020; Long, Xie, et al., 2020; Long et al., 2018). The responses of the ocean to external RF can be split into two components: fast response and slow response (Dickinson, 1981; Held et al., 2010; Manabe et al., 1990; Stouffer, 2004). The fast response is the response of the ocean mixed layer to the change in external RF by rapidly exchanging energy with the atmosphere and deep ocean; and the slow response is the slow evolution of temperature in the deep ocean which has great thermal inertia and leads to the redistribution and adjustment of heat between the upper and deeper ocean (Long et al., 2014). These two processes have different climatic responses to oceanic stratification, ocean currents (the meridional overturning circulation [MOC] in Southern Ocean and North Atlantic Ocean) and sea surface temperature (SST; Long, Xie, et al., 2020; Long et al., 2014). During RF increase, climatic responses are mainly the effects of the fast response; after RF stabilization, the effects of the interior of the ocean will be more important (Long, Xie, et al., 2020).

As the source of global water vapor, the ocean plays a key role in the global water circulation system. The tropical Indian Ocean (IO) is an important part of the underlying surface of the Asian-Australian monsoon region, its air-sea interaction influences the Asian-Australian monsoon and even the global climate. Previous studies have focused on the rainfall response over the tropical IO during RF increase (Ma et al., 2018; Qu et al., 2015; Xie et al., 2010), while less attention has been given to its change after RF stabilization. Therefore, this research focuses on rainfall changes over the tropical IO under global warming and reveals how fast and slow responses affect rainfall.

Interestingly, the rainfall responses over the tropical IO exhibit large distinctions during RF increase and stabilization (Figure 1). During RF increase, rainfall is enhanced over the tropical northern IO, the Indian Peninsula and the Bay of Bengal and decreases over the southeastern IO (Figure 1a; Qu et al., 2015). It also shows good intermodel consistency among the models (stippling in Figure 1a). After RF stabilization, the pattern of the rainfall response over the IO is totally different. It is enhanced over the southwestern IO but reduced over the northern IO and Maritime Continent (Figure 1b). These different rainfall responses during the two periods are interesting, and the associated mechanism is revealed in this research. To quantify the rainfall changes, we select two boxes in each rainfall response that are located at values with larger rainfall change (Figure 1). An increasing number of countries and regions are taking action to reduce carbon emissions, and the understanding of climatic responses after RF stabilization is an important issue in climate change research.

The rest of the paper is organized as follows. Section 2 introduces the data and methods used in this study. Section 3 presents the diagnostic analysis of rainfall and SST patterns and proposes a theoretical framework for rainfall changes. Section 4 provides the discussion and summary.

2. Data and Methods

2.1. Data

The present study is based on the Coupled Model Intercomparison Project Phase 5 (CMIP5) monthly outputs (Table 1). The experiments used are: (a) historical, which is forced by observed anthropogenic and natural forcing from 1850 to 2005; and (b) the RCP4.5 experiment, in which the RF gradually increases to 4.5 W m^{-2} until 2100 and then stabilizes during 2100–2300 (Figure 2). In the latter experiment, the output

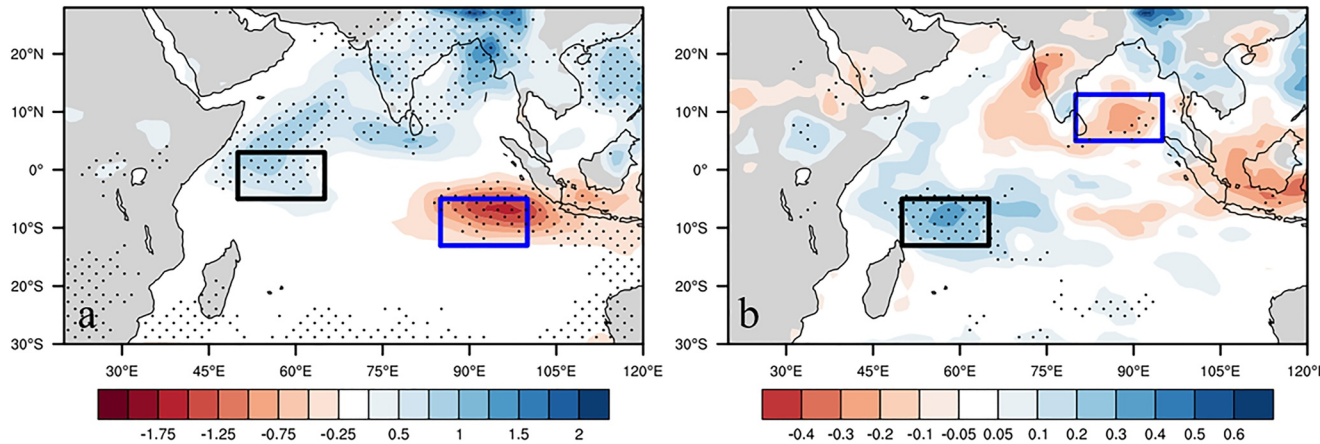

Figure 1. The responses of rainfall (units: mm d^{-1}; color shading) during the radiative forcing (RF) increase (a) and stabilization (b). Stippling indicates that more than 80% of the models (10 out of 13) agree on the sign of the multi-model ensemble (MME) results. The black and blue boxes in panels (a, b) are used for diagnostic analysis of the sea surface temperature (SST) pattern in Section 3.3 and Figure 11.

after 2100 is also named the Extended Representative Concentration Pathways scenario 4.5 experiment (ECP4.5, Sniderman et al., 2019). The present study uses the outputs of 13 models in which the entire results of ECP4.5 are available. Detailed information can be found on the official website: http://cmip-pcmdi.llnl.gov/cmip5/. As these models have different resolutions, all outputs are interpolated onto 1.0° latitude × 1.0° longitude. We use the results of multi-model ensembles (MMEs) to reduce the effect of climate internal variability. We only use the first member (r1i1p1) of each model for analysis. Note that, the RCP8.5 simulations in CMIP5 also have outputs extending to 2300, but the stability phase is only several decades rather than 200 years in the RCP4.5 simulations. Considering that the stability phase is not long enough to be used to calculate the responses according to the criteria in context behind and that the stability phase is too short to reveal the ocean slow response, the RCP8.5 simulation is not used in present paper. In addition, as only the outputs of four models in the Coupled Model Intercomparison Project Phase 6 (CMIP6) are available for the present study, they are not adopted in the present study, too.

Table 1
List of CMIP5 Models and Their Missing Variables

No.	Model name	Institute	Missing variables
1	bcc-csm1-1	Beijing Climate Center, China Meteorological Administration, China	
2	CanESM2	Canadian Centre for Climate Modelling and Analysis, Canada	wmo
3	CESM1-CAM5	National Center for Atmospheric Research, USA	sfcWind, uas, vas
4	CNRM-CM5	Centre National de Recherches Météorologiques, Centre Européen de Recherche et de Formation Avancée en Calcul Scientifique, France	
5	CSIRO-Mk3.6.0	Commonwealth Scientific and Industrial Research Organization in collaboration with Queensland Climate Change Centre of Excellence, Australia	
6	FGOALS-s2	LASG, Institute of Atmospheric Physics, China	wmo, hurs, thetao
7	GISS-E2-H	NASA/GISS Goddard Institute for Space Studies, USA	wmo
8	GISS-E2-R		
9	IPSL-CM5A-LR	Institute Pierre Simon Laplace, France	
10	IPSL-CM5A-MR		
11	MIROC-ESM	Atmosphere and Ocean Research Institute (The University of Tokyo), National Institute for Environmental Studies, and Japan Agency for MIROC5 Marine-Earth Science and Technology, Japan	wmo
12	MPI-ESM-LR	Max Planck Institute for Meteorology, Germany	hurs
13	NorESM1-M	Norwegian Climate Centre, Norway	sfcWind

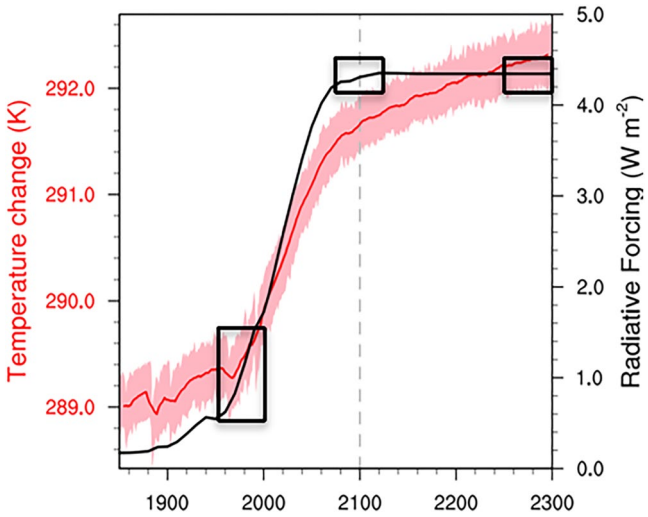

Figure 2. Time series of the global mean surface temperature (units: K; red line, removing 11-year-moving average) and RF pathways (units: W m^{-2}; black line). The light pink shading indicates 1 standard deviation of inter-model variability. The gray vertical dashed line is the turning point of RF. The black boxes are three windows (1956–2005, 2076–2125, and 2251–2300) used in the present research to analyze climatic responses during RF increase and stabilization.

The performance of CMIP5 results in simulating rainfall over the northern IO is evaluated against the Global Precipitation Climatology Project (GPCP) monthly rainfall outputs (Adler et al., 2003) in 1979–2005. The simulation of the mixed layer depth (MLD) from CMIP5 MME is compared with the other three reanalysis results, Ocean Mixed Layer Depth Climatology, ECMWF Ocean Reanalysis System 5 (ORA-S5) opa0 and the Simple Ocean Data Assimilation ocean/sea ice reanalysis Version 3 (SODA3; Carton et al., 2018), in 1980–2005. In CMIP5, the MLD is defined as the 0.2°C cooling referenced to the potential temperature at 10 m depth. The analysis focuses on the average in boreal summer (June–August) because ~80% of annual rainfall is in the summer period in IO.

As 2100 is the RF inflection point when RF changes from increasing to stabilizing, we choose 2100 as the center of the period used to separate the two responses (Figure 2). The climate feedback of RF increase is defined as the mean of 2076–2125 (ECP4.5 experiment) minus the mean of 1956–2005 (historical experiment); the response during the RF stabilization is the mean of 2251–2300 minus the mean of 2076–2125. These three periods are shown as black boxes in Figure 2. The basic states of the two periods are defined as the mean of 1956–2005 in the historical experiment and the mean of 2076–2125 in the ECP4.5 experiment. We also slightly altered the beginning years of the periods and obtained similar results.

2.2. The Linear Baroclinic Model Simulation

The linear baroclinic model (LBM) is used in the present study to understand the atmospheric responses to heating (Ma et al., 2012; Qu et al., 2015). The model is composed of atmospheric primitive equations (Watanabe & Kimoto, 2000) and linearizes them to grasp the atmospheric response to forcing. It can analyze the linear dynamics in the atmosphere by computing steady linear responses to a prescribed forcing, eigenanalysis, and so on. In the present study, we utilized the steady forcing to study the influence of heating on surface wind and vertical circulation. The model resolution is T42 in the horizontal direction and 20 sigma (σ) in the vertical direction. The climatology of the model uses the CMIP5 MME in the climatology of the RF increase (1956–2005) and stabilization (2076–2125) periods. The horizontal diffusion has an *e*-folding decay time of 6 hr for the largest wavenumber. The Rayleigh friction and Newtonian damping have a time-scale of 1 day^{-1} for $\sigma > 0.9$ and $\sigma \le 0.02$, 5 $days^{-1}$ for $\sigma = 0.9$, 15 $days^{-1}$ for $\sigma = 0.8$ and 30 $days^{-1}$ for $0.02 < \sigma < 0.8$. And the vertical diffusion is set at 1,000 $days^{-1}$ at all levels. The model is integrated for 50 days to gain a steady situation, and we choose the mean results of 30–50 days as displayed. In addition, as the external forcing after RF stabilization is too small to counteract the internal perturbations of the model, the forcing multiplied by 10 forces the model to reach its magnitude in the RF increase, and the results are finally divided by 10. The forcing patterns after RF stabilization are shown in Figure S4 in Supporting Information S1. We also compared the LBM simulation results in which the forcings are multiplied by 1–10, respectively, during the RF stabilization. It is found that the response pattern is more stable after forcing amplification of 6–10 times. All of these five experiments show similar responses. The responses in which forcings are multiplied by 1–5 vary greatly due to the noise, so they are not adopted. For convenience, we use the results with forcings amplification of 10 times in main text.

2.3. Moisture Budget

The rainfall pattern under global warming can be written as, following Qu et al. (2015):

$$P_r' = -\langle \bar{\omega}\partial_p q' \rangle - \langle \omega' \partial_p \bar{q} \rangle - \langle \bar{\vec{V}} \cdot \nabla q' \rangle - \langle \vec{V}' \cdot \nabla \bar{q} \rangle + R_{Pr}' + E' \quad (1)$$

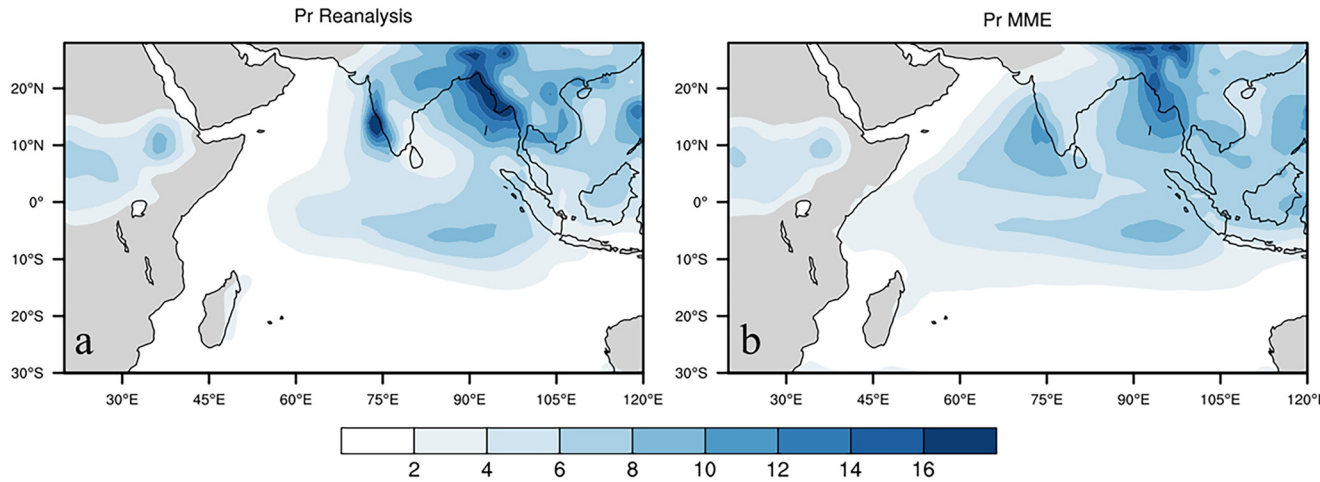

Figure 3. The climatology of rainfall over the Indian Ocean (IO; units: mm d^{-1}; color shading) in 1979–2005. Panel (a) shows the Global Precipitation Climatology Project (GPCP) monthly rainfall outputs, and panel (b) shows the MME results of the Coupled Model Intercomparison Project Phase 5 (CMIP5) historical experiment.

where the overbar and prime denote the climatology and change during the RF increase and stabilization, respectively. Here, P_r is the rainfall, ω is the pressure velocity, P is the pressure, q is the specific humidity, $\vec{V}$ is the horizontal velocity, E is the evaporation, $R_{Pr}^{'}$ is the quadratic terms, and $\langle\rangle$ represents mass integration from the surface to 100 hPa.

2.4. Anomalous Vertical Velocity Due to Heating

The anomalous vertical velocity due to heating can be written as (Ma et al., 2012):

$$B\omega'\frac{\partial\overline{\theta}}{\partial p} = -B\overline{\omega}\frac{\partial\theta'}{\partial p} + Q_1^{'} \tag{2}$$

where $B = \frac{T}{\theta} = \left(\frac{p}{p_s}\right)^{\frac{R_{\text{dry}}}{C_p}}$, p_s is the surface pressure, p is the pressure, R_{dry} is the gas constant for air, and θ is the potential temperature. The apparent heat source Q_1 is (Yanai et al., 1973):

$$Q_1^{'} = C_p\left(\overline{\vec{V}}\cdot\nabla T' + \vec{V}'\cdot\nabla\overline{T} + B\overline{\omega}\frac{\partial\theta'}{\partial p} + B\omega'\frac{\partial\overline{\theta}}{\partial p}\right) \tag{3}$$

where C_p is the specific heat at constant pressure and T is the air temperature. The mean advection of stratification (called "stratification" for short) can be written as (Ma & Xie, 2013; Ma et al., 2012, 2018):

$$Stratification = -B\overline{\omega}\frac{\partial\theta'}{\partial p} \tag{4}$$

2.5. Performance of the CMIP5 Rainfall Simulation

Before analyzing the changes in rainfall over the IO during RF increase and stabilization, we compared the climatological rainfall of the GPCP with that of historical experiment in CMIP5. The focused period is 1979–2005. In boreal summer, the GPCP results exhibit heavy rainfall over South Asia with two major centers: one is in the Bay of Bengal and Indo-China Peninsula, and the other is on the west coast of the Indian Peninsula (Figure 3a). The CMIP5 MME can grasp the spatial distribution, but the amount of rainfall is slightly weak (Figure 3b). The spatial correlation coefficients of individual model with GPCP all exceed 0.58 (Figure 4). In general, the CMIP5 MME reproduces the rainfall distribution over the tropical IO well in

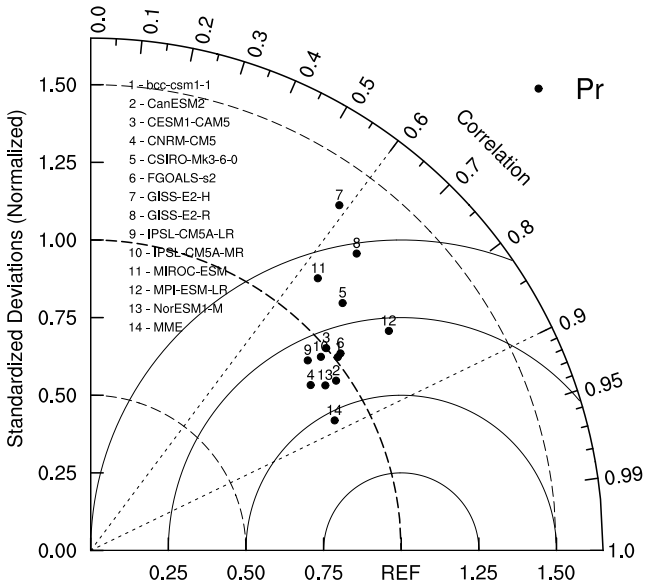

Figure 4. Taylor diagram of the rainfall change over the IO from CMIP5 MME simulations compared with the GPCP outputs during 1979–2005. The reference point is the GPCP results. The numbers 1–13 denote the model's serial numbers in Table 1, and the last 14 denotes the result of CMIP5 MME.

climatology, whose pattern correlation coefficient with the observation is 0.88. Thus, the CMIP5 MME is capable of studying the rainfall response to the RF changes.

3. The Change in Rainfall Response Over the IO

During RF increase, the change in rainfall pattern displays a northwest-southeast dipole over the IO, while it changes into a southwest-northeast dipole after RF stabilization. These two different rainfall responses during RF increase and stabilization, as mentioned in the Section 1, are associated with their underlying SST patterns, which agrees with the "warmer-get-wetter" mechanism (Long et al., 2014; Xie et al., 2010). During RF stabilization, much heat is absorbed by the deep ocean, especially in the Southern Ocean, where warming expands from 500 m to the bottom and varies the SST pattern (Figure 5; Long, Liu, et al., 2020; Long, Xie, et al., 2020). The warming in the Southern Hemisphere is greater than that in the Northern Hemisphere, and the most apparent warming is found over the Southern Ocean. This change in the warming pattern may lead to different rainfall responses from the past, and the increasing rainfall ceases over the northern IO after RF stabilization. Besides, the SST responses of individual model simulations are shown in Figures S1 and S2 in Supporting Information S1, and the pattern correlation coefficients of SST change in individual model results with those in the CMIP5 MME are all reaching the 95% significance level over the IO (30°S–28°N,

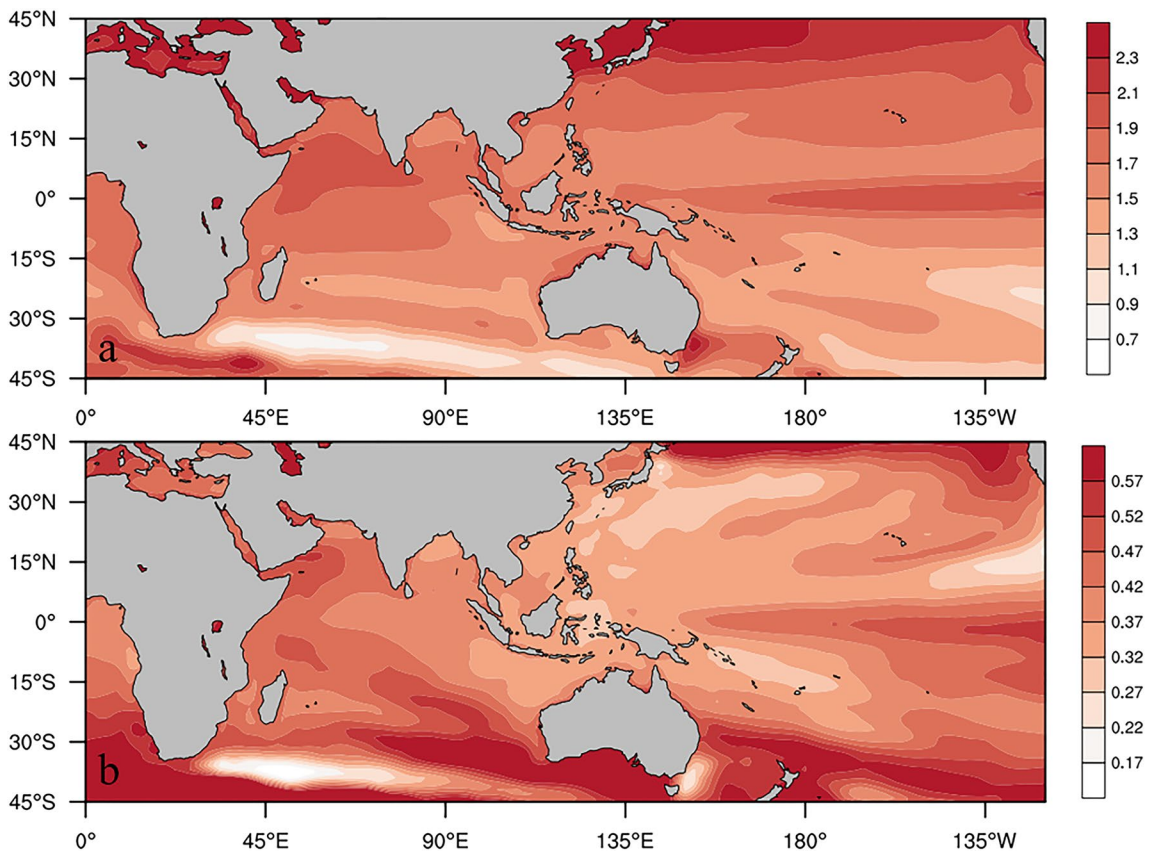

Figure 5. The responses of the SST pattern (units: K; color shading) during the RF increase and stabilization. Panel (a) shows the pattern during RF increase and panel (b) shows the pattern after RF stabilization. All results are based on the CMIP5 MME. The model consistency is not shown for clarity.

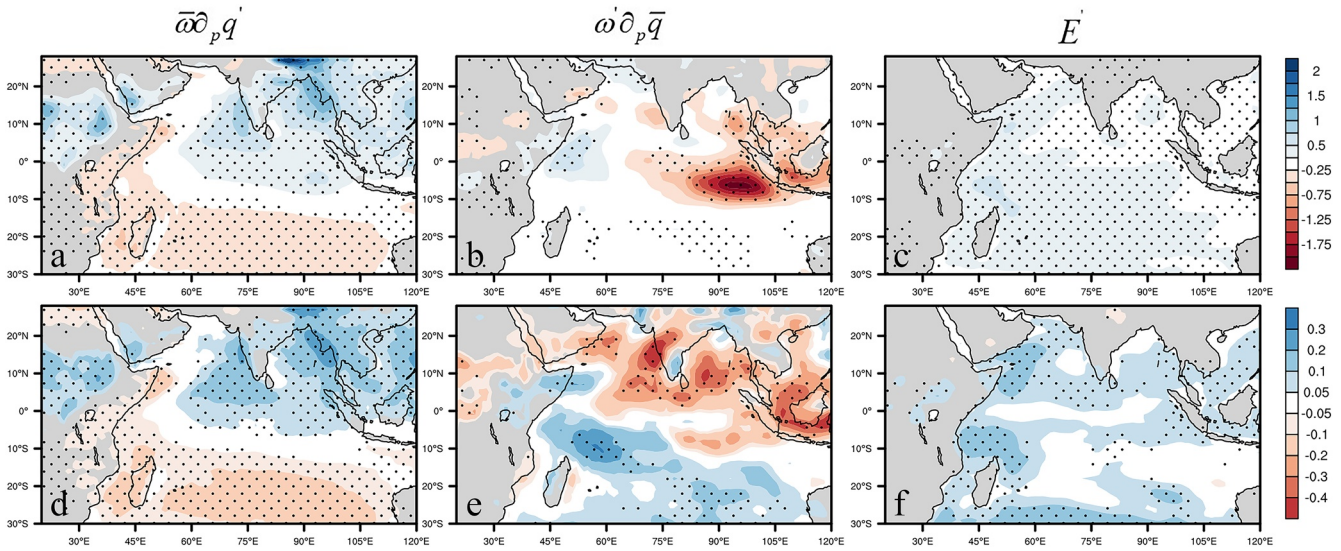

Figure 6. Distributions of the mass integration of the vertical transport and evaporation change of the moisture budget (units: mm d^{-1}; color shading). Panels (a, d) are the results of the vertical gradient of humidity change transported by climatological vertical velocity, $\overline{\omega}\partial_p q'$; panels (b, e) are the results of the vertical gradient of climatological humidity transported by vertical velocity change, $\omega'\partial_p \overline{q}$; and panels (c, f) are the evaporation responses. Panels (a–c) are the results during RF increase, and panels (d–f) are the results during RF stabilization. All of them are based on the CMIP5 MME, and stippling indicates that more than 80% of the models (10 out of 13) agree on the sign of the CMIP5 MME results.

30°–120°E) during RF increase and stabilization. The attributions of rainfall change are revealed in the following section.

3.1. Rainfall and Atmospheric Circulation

The terms of the diagnostic equation of rainfall changes, as shown in Equation 1, are analyzed to understand the rainfall responses during RF increase and stabilization. Figure 6 displays the contributions of the two vertical terms and the evaporation change during RF increase and stabilization; because of the small contributions, the horizontal terms and the quadratic terms are not displayed. During RF increase, the vertical gradient of climatological humidity transported by vertical velocity change, $\omega'\partial_p \overline{q}$, over the IO features a northwest-southeast dipole response, while after RF stabilization, the term displays a southwest-northeast dipole structure (Figures 6b and 6e). The term of the vertical gradient of humidity change transported by climatological vertical velocity, $\overline{\omega}\partial_p q'$, shows a similar northeast-southwest asymmetry during the two periods, but it becomes weaker after RF stabilization (Figures 6a and 6d). Evaporation is slightly enhanced over the tropical IO during both RF increase and stabilization (Figures 6c and 6f). By comparing the diagnostic results, it is found that the patterns of rainfall change are mainly due to the term of the vertical gradient of climatological humidity transported by vertical velocity change, $\omega'\partial_p \overline{q}$ (Figures 6b and 6e). That is, the changes in vertical motion mainly lead to the two kinds of rainfall responses over the IO.

The attributions contributing to rainfall patterns display some discrepancies depending on region. During RF increase, the moisture response increases more in the lower troposphere than in the upper troposphere (Figure S3 in Supporting Information S1; Richter & Xie, 2008). The rainfall increases over the northern IO which is mainly due to thermodynamic (moisture) changes (Figure 6a); the increase change over the east coast of Africa and the decrease over the southeastern IO are mainly the results of dynamic circulation (Figure 6b). Both effects are important to the pattern of rainfall change during this period. However, after RF stabilization, the contributions are different. Because of the tiny change in atmospheric humidity, the effect of dynamic circulation contributes more. This southwest-northeast dipole of rainfall change is mainly led by dynamic circulation changes (Figure 6e). In general, the pattern of rainfall change is mainly due to a dynamic circulation response rather than an increase in thermodynamic moisture. This result is consistent with the "warmer-get-wetter" mechanism (Bony et al., 2013; Chadwick, Boutle, & Martin, 2013; Richardson et al., 2016; Ma et al., 2018; Seager et al., 2010).

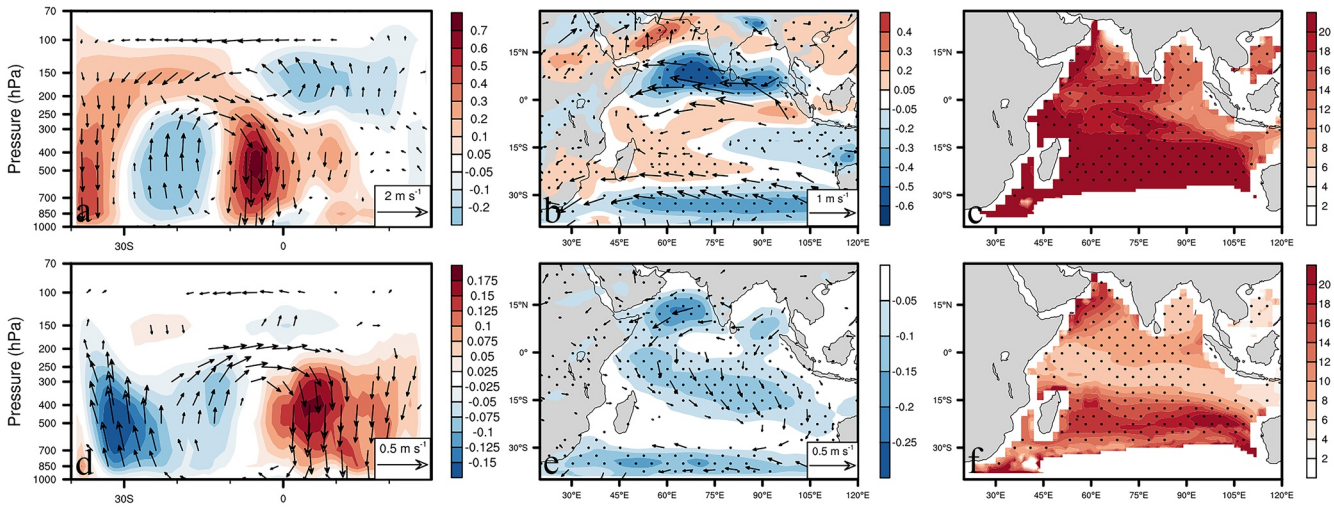

Figure 7. The responses of the anomalous vertical circulation (a, d), surface wind (b, e), and thermocline depth (c, f) over the IO (40°S–28°N, 40°–120°E) during RF increase (a–c) and stabilization (d–f). (a, d) The color shading indicates the vertical velocity changes (units: 1.0^{-2} Pa s^{-1}), the pressure velocity is multiplied by −200, and the wind anomalies at 80% model consistency are displayed with vectors. (b, e) The scalar surface wind is shown in color shading (units: m s^{-1}), and stippling indicates that more than 80% of the models (10 out of 13) agree on the sign of the CMIP5 MME results. The thermocline depth is defined as the depth of the isothermal surface at 20°C. In addition, only the surface wind vector changes exceeding 80% model consistency are shown. All results are based on the CMIP5 MME.

As anomalous vertical velocity is crucial in determining rainfall patterns, we further explored the causes of changes in vertical velocity. Anomalous atmospheric ascent exists where SST warming exceeds the tropical mean and leads to the enhancement of convective rainfall, and anomalous descent occurs where SST warming is less than the tropical mean (Figures 5 and 7a,7d; Long et al., 2014; Ma et al., 2018; Qu et al., 2015; Xie et al., 2010). During RF gradual increase, the greater warming of SST is accompanied by anomalous easterlies over the northern and equatorial IO (Figure 7b). It reduces the southwesterly monsoon over the tropical northern IO and enhances the easterly trade winds over the tropical southern IO (Qu et al., 2015). Reduced scalar surface wind leads to the suppressed evaporation of the tropical northern IO, which favors SST warming, and vice versa to the south (Figures 6c and 7b). Anomalous easterly winds also contribute to the water pile up to the west and deepen the thermocline, forming an east-west gradient of the equatorial thermocline (Figure 7c). As RF increases, the zonal average of the vertical velocity over the IO features an apparent descent south of the equator. This wind-evaporation-SST (WES) feedback is a vital positive feedback that may amplify the initial disturbance (Qu et al., 2015; Xie et al., 2010). After RF stabilization, the SST warming is relatively slow over the northeastern IO but faster over the western IO; this zonal SST gradient leads to the northerlies response over the northern IO (Figures 5b and 7e). The thermocline south of 10°S deepens (Figure 7f), and the reason for this phenomenon will be analyzed in Section 3.3. The atmosphere features an overturning circulation with anomalous ascent over the warmer ocean and anomalous descent north of equator (Figure 7d). Although the thermodynamic effect (the effect of atmospheric moisture) plays an important role in regional rainfall change, the circulation response contributes increasingly to the patterns of rainfall change and partly offsets the thermodynamic effects (Chadwick, Boutle, & Martin, 2013; Ma et al., 2018; Seth et al., 2019; Wang et al., 2014). In the next section, the mechanism about how SST warming influence atmospheric movement is studied.

3.2. The Effects of Stratification and Diabatic Heating on Atmospheric Circulation

The SST influences the anomalous vertical velocity mainly by two processes based on Equation 2: the apparent heat source (Q_1) and the mean advection of stratification (called "stratification" for short). The uniform warming of the ocean can warm the atmosphere above and lead to changes in atmospheric stratification; inhomogeneous SST warming causes anomalous ascent and descent according to the "warmer-get-wetter" mechanism. Stratification more recently revealed the role of atmospheric warming in circulation slowdown (Ma & Xie, 2013; Ma et al., 2012, 2018). The upper troposphere warms more than the lower troposphere in

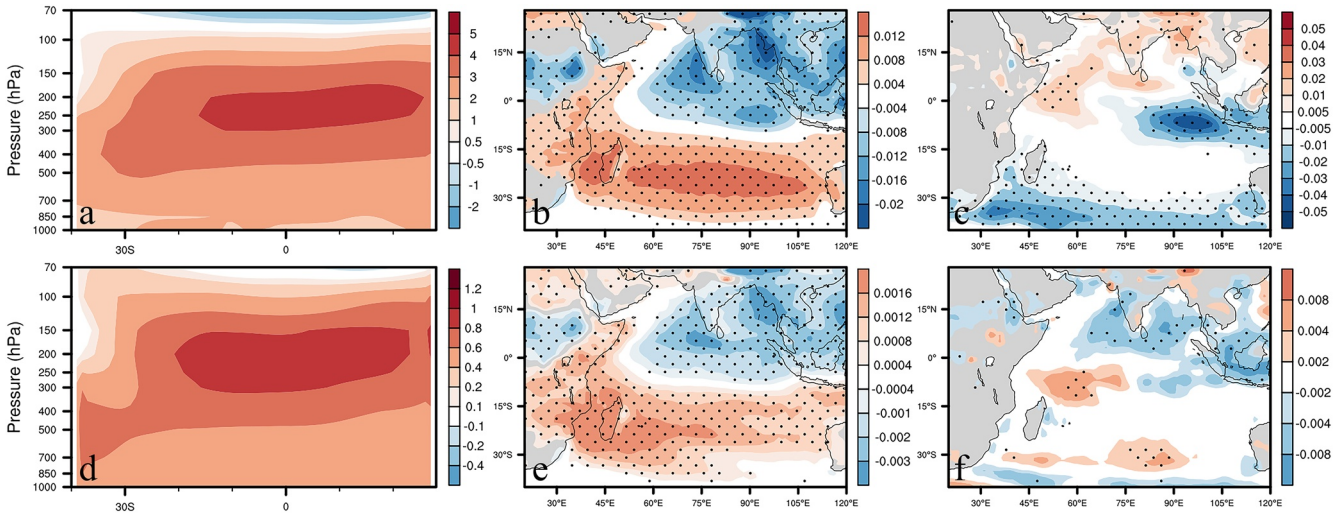

Figure 8. The zonal average of the temperature response between 40°–120°E (units: K; color shading) and the mass integration of the mean advection of stratification patterns and the apparent heat source patterns from surface to 300 hPa (units: K kg s^{-1} m^{-2}; color shading) during the RF increase (a–c) and stabilization (d–f). Panels (a, d) show temperature responses, panels (b, e) show the mean advection of the stratification patterns, and panels (c, f) show the apparent heat source patterns. All results are based on the CMIP5 MME. Stippling in panels (b, c, e, f) indicates that more than 80% of the models (10 out of 13) agree on the sign of the CMIP5 MME results. The model consistency is not shown in panels (a, d) for clarity.

the tropics under global warming (Knutson & Manabe, 1995; Wang et al., 2014), resulting in an anomalous sinking motion (Figures 8a and 8d). The effect of stratification acting as a forcing opposes the climatological circulation and slows atmospheric circulation (Ma et al., 2018). It displays anomalous cooling over the northern IO and warming over the southern IO (Figures 8b and 8e). The changes in stratification are weaker between the two periods. Stratification predicts a drying trend of rainfall over regions with strong climatological ascent, which opposes the effects of the thermodynamic (humidity) effect (Ma et al., 2018).

The patterns of Q_1 are similar to rainfall responses during the two periods (Figures 8c and 8f). It displays northwest-southeast asymmetry during RF increase but a southwest-northeast dipole structure after RF stabilization. Next, we use the spatial distribution of the stratification and Q_1 in the CMIP5 MME to force the LBM and analyze their effects on atmospheric circulation. As displayed in the former section, anomalous atmospheric movement is sensitive to the SST response. In this section, we analyze the causes of atmospheric circulation change by forcing the LBM. Ma et al. (2012) noted that both the stratification effect and diabatic heating should be considered in a fully coupled model to reproduce the responses of atmospheric circulation under global warming, while this stratification effect is not included by default. We used both effects to force the LBM.

The key responses of atmospheric circulation during RF increase and stabilization are well reproduced by the LBM forced by the two effects. During RF increase, the two forcings reproduce the following responses in the CMIP5 MME: anomalous descent near the equator IO and south of 30°S in the mid- and lower troposphere, the descent anomaly over the southern IO in the upper troposphere, the anomaly weak ascent over the northern IO in the upper troposphere and 30°–20°S (Figures 7a and 9c), and the anomalous surface easterlies over the IO (Figures 7b and 10c). During RF stabilization, the key responses of atmospheric circulation in the CMIP5 MME are all captured by the LBM forced by the two effects. The key responses include anomalous ascent (descent) over the southern (northern) IO in the lower troposphere, anomalous overturning over the tropical southern IO and equatorial IO in the upper troposphere (Figures 7d and 9f), and anomalous surface northerlies (Figures 7e and 10f). Thus, it is trustworthy to use the LBM to investigate the individual effects of apparent heating and stratification.

During RF increase, the apparent heating yields anomalous ascent over the northern IO and anomalous descent south of the equator (Figure 9a); however, it does not reproduce the anomalous ascent over 30°–20°S in the CMIP5 MME. Easterlies exist over the northern IO (Figure 10a). The results forced by the stratification effect display totally different patterns; there is anomalous ascent over the southern IO but descent over

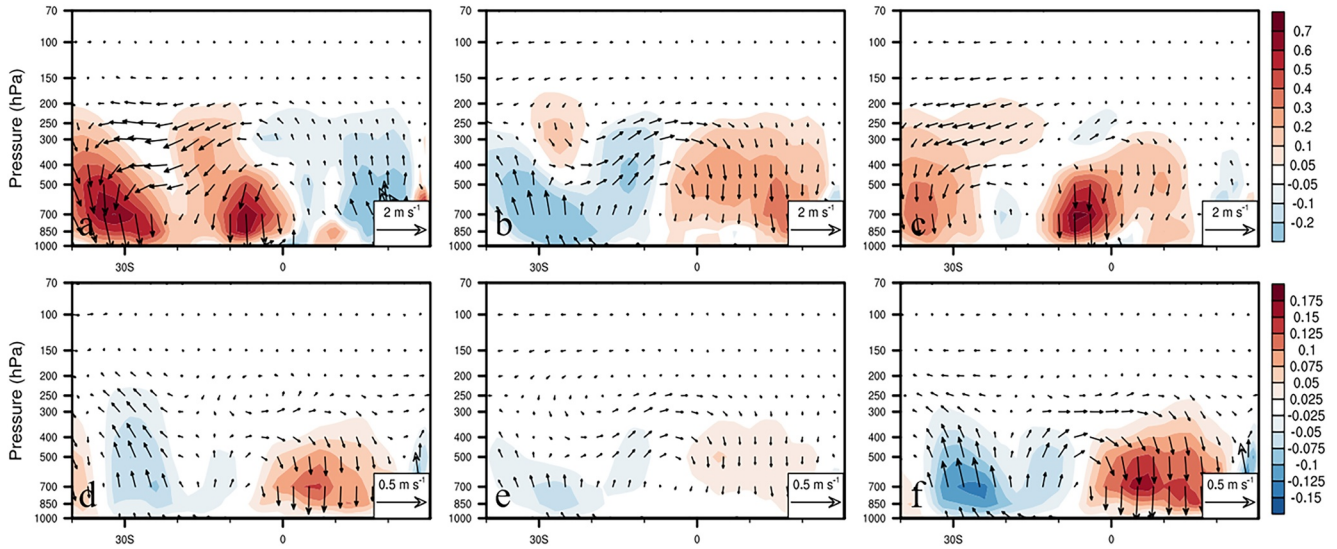

Figure 9. As in Figures 7a and 7d, but for the responses in the linear baroclinic model (LBM) forced by the apparent heat source and the mean advection of stratification pattern and both of them during the RF increase (a–c) and stabilization (d–f). Panels (a, d) are the results of apparent heat source, panels (b, e) are the results of the mean advection of stratification, and panels (c, f) are the results considering both of them.

the northern IO (Figure 9b) and anomalous northerlies over the northern IO (Figure 10b), which offsets the influence of diabatic heating. This phenomenon indicates that the effects of diabatic heating and stratification are both crucial to atmospheric circulation, and the stratification on behalf of the circulation slowdown counteracts the wetter trend over the northern IO.

After RF stabilization, the roles of diabatic heating and the stratification effect are similar. Both of them yield anomalous ascent south of the equator, anomalous descent north of the equator (Figures 9d and 9e), and surface northerlies across the IO (Figures 10d and 10e). The effects of both are consistent during this period, very different from those during RF increase, in which the effects of stratification partly offset those of diabatic heating on atmospheric wind.

The SST response may lead to changes in atmospheric circulation, diabatic heating and stratification; the changes in diabatic heating and stratification may modify the atmospheric circulation and the underlying

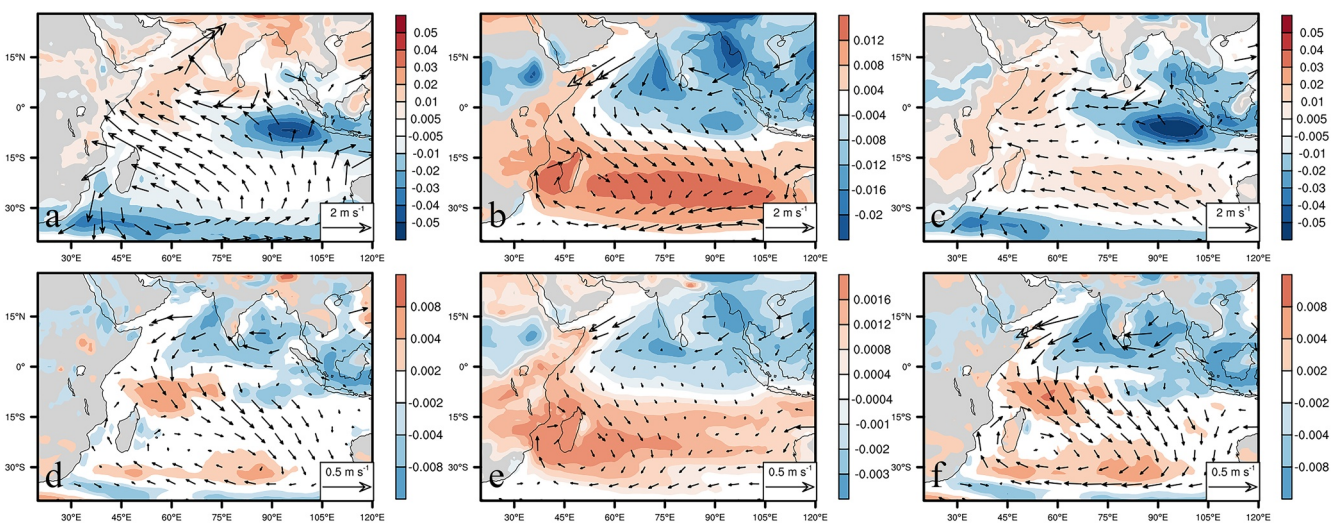

Figure 10. As in Figure 9, but for the response of surface wind (vectors) and the mass integrations of the forcings (color shading; units: K kg s^{-1} m^{-2}) from the surface to 300 hPa. The forcings are the apparent heat source (a, d), the mean advection of stratification (b, e), and the sum of the two (c, f).

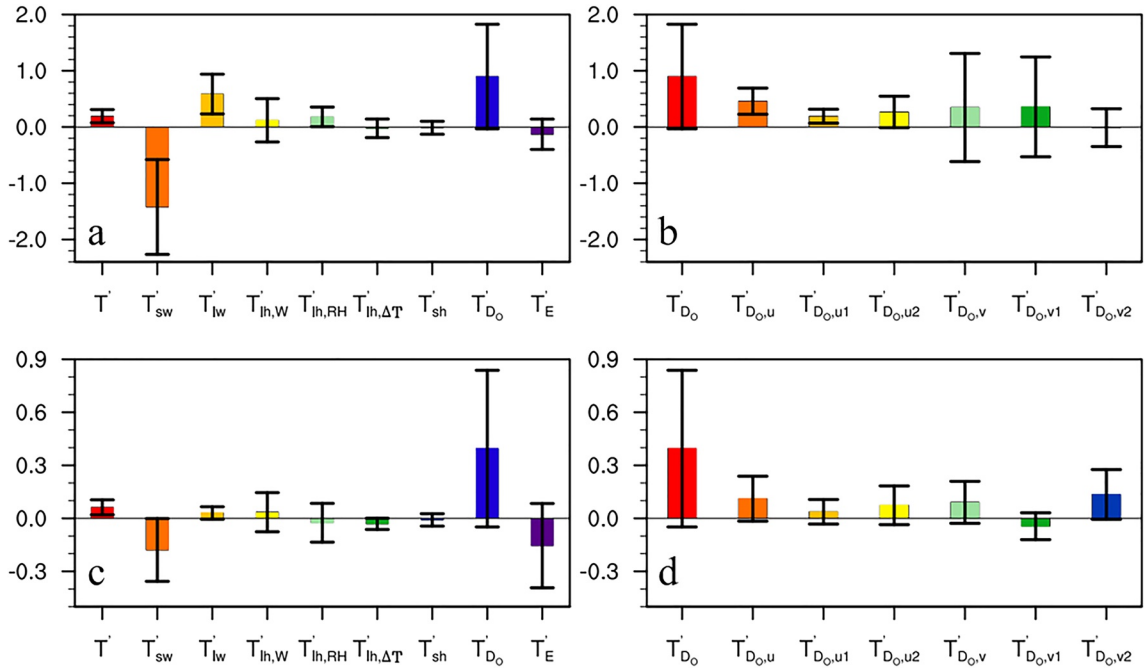

Figure 11. Diagnostic results of the formation of SST asymmetry (units: K) during RF increase (a, b) and stabilization (c, d) using a fixed MLD, 50 m. Anomalous SST asymmetry in the northern IO is the SST response in the black box (5°S–3°N, 50°–65°E) minus the blue box (13–5°S, 85°–100°E) during RF increase; after RF stabilization, it is the black box (13°–5°S, 50°–65°) minus the blue box (5°–13°N, 80°–95°E). See Equations S1–S16 in Supporting Information S1 for details of calculations and the definition of each term. (a, c) The SST changes (T') and the attributions to the SST patterns are the changes in net shortwave radiation (T'_{sw}), the changes in net longwave radiation (T'_{lw}), the changes in net latent heat flux due to surface wind ($T'_{lh,W}$), relative humidity ($T'_{lh,RH}$) and surface stability ($T'_{lh,\Delta T}$), the changes in net sensible heat flux (T'_{sh}), the quadratic term of the evaporation change (T'_E), and ocean dynamics (T'_{D_O}). (b, d) The contribution of ocean dynamics to the formation of the SST pattern is further divided into changes in zonal ($T'_{D_O,u}$) and meridional ocean heat transport ($T'_{D_O,v}$), and both of them include changes in ocean currents ($T'_{D_O,u1}$ and $T'_{D_O,v1}$) and changes in ocean temperature gradients ($T'_{D_O,u2}$ and $T'_{D_O,v2}$).

SST. Thus, the responses of the SST, atmospheric circulation, diabatic heating, and stratification over the IO are well coupled.

3.3. The Formation of the SST Pattern

In the former sections, we revealed that the differences in SST patterns favor anomalous atmospheric movement to display diverse patterns of rainfall change during RF increase and stabilization. There is a northwest-southeast SST gradient over the northern IO when the RF gradually increases (Figure 5a), while, it warms more in the southwestern IO than in the northeastern IO after RF stabilization, it looks like the letter C (following called "C-type warming asymmetry"; Figure 5b). To further evaluate the SST responses, a diagnostic analysis of the ocean mixed layer energy budget is conducted. The mixed layer energy budget can be written as:

$$C\frac{\partial T'}{\partial t} = Q'_{net} + D'_O \tag{5}$$

where $C = \rho_o C_p H$ is the heat capacity of the mixed layer, H is the MLD, here, we define the MLD as the fixed 50 m and also compare the results between the fixed and varying MLD (Figure 11 and S7 in Supporting Information S1). Q'_{net} is net surface flux into the ocean (downward is positive), D'_O is the ocean dynamics effect due to advection, diffusion and mixing, T' is SST change, and the term on the left side of the equation is close to 0 in a long-term mean (Deser et al., 2010; Hwang et al., 2017; Kang et al., 2020; Xie et al., 2010; Ying et al., 2016). A more detailed derivation can be found in the Supporting Information S1. The climatological states of MLD simulated from the individual model and MME are shown in Figure S6 in Supporting Information S1, and we also compare the results of CMIP5 MME with the other three reanalysis (Ocean Mixed Layer Depth Climatology, ECMWF ORA-S5, and SODA3) in 1980–2005 (Figure S5 in

Supporting Information S1). The MLD is shallower in northern IO and deeper in the southern IO (Figures S5b–S5d in Supporting Information S1), which is reproduced by CMIP5 MME (Figure S5a in Supporting Information S1). But the CMIP5 MME result display shallow bias in northern IO.

Following Hwang et al. (2017) and Ying et al. (2016), the changes in SST can be written as:

$$T' = T'_{sw} + T'_{lw} + T'_{lh,W} + T'_{lh,RH} + T'_{lh,\Delta T} + T'_{sh} + T'_{E} + T'_{D_O,u1} + T'_{D_O,u2} + T'_{D_O,v1} + T'_{D_O,v2} + T'_{D_O,w1} + T'_{D_O,w2} + T'_{O} \quad (6)$$

The change in SST is decomposed into the effects of shortwave radiation, longwave radiation, and latent heating due to the changes in surface wind, surface relative humidity and ocean-atmosphere stability, sensible heat flux, and ocean heat transport in three dimensions. To quantify the enhanced warming, the SST changes over the northern IO are computed as the greater warming area (black box) minus the suppressed warming area (blue box) during RF increase and stabilization in Figure 1. Figure 11 displays the differences of each term in Equation 6 and the SST change between the greater warming area and weaker warming area (positive values represent greater warming in the defined "warming area"). The vertical heat transport term and residual ocean heat transport term have less contribution; therefore, they are not displayed. As the results between the fixed and spatially nonuniformed MLD are similar, here a fixed depth of 50 m of MLD is used (Figure 11 and S7 in Supporting Information S1). Besides, a fixed depth of MLD (50 m) can simplify the calculation as the MLD among the models is different (Figure S6 in Supporting Information S1; Ng et al., 2015). Note that the term net shortwave radiation T'_{sw} is associated with cloud change, which is a complicated process, thus, we do not discuss it here.

During RF increase, there is greater warming over the northwestern IO but less warming over the southeastern IO (Figure 5a). The changes in longwave RF, T'_{lw}, and ocean dynamics, T'_{D_O}, which are mainly led by ocean heat transport due to ocean current changes in zonal and meridional directions, $T'_{D_O,u1}$ and $T'_{D_O,v1}$, mainly contribute to this northwest-southeast SST asymmetry (Figure 11b). Ocean currents are the result of ocean surface wind stress and atmospheric circulation (Vecchi & Soden, 2007; Ying et al., 2016), and they feature northerlies over the northern IO in climatology (vectors in Figure S8a in Supporting Information S1). In the northern tropical IO, anomalous southeasterly currents transport heat westward and enhance warming here; in addition, in the southeastern IO, anomalous easterly currents cool the ocean surface (shading in Figure S8a and vectors in Figure S8b in Supporting Information S1). The zonal ocean heat transport due to the temperature change, $T'_{D_O,u2}$, is also in favor of this northwest-southeast asymmetry in which northerly currents over the northern IO in climatology with warmer temperatures lead to greater warming over the northwestern IO (vectors in Figure S8a and shading in Figure S8b in Supporting Information S1).

After RF stabilization, the ocean in the southwestern IO warms more than that in the northeastern IO, similar to C-type warming (Figure 5b), which is a result of deeper ocean influence. This southwest-northeast SST asymmetry is mainly due to changes in ocean dynamics (T'_{D_O}, mainly led by ocean heat transport due to temperature changes in the zonal and meridional direction, $T'_{D_O,u2}$ and $T'_{D_O,v2}$, respectively). The northeasterly currents over the northern IO and southwesterly currents over the Southern Ocean in climatology lead to heat convergence over the southwestern IO while cooling the sea surface over the northeastern IO (vectors in Figure S8a and color shading in Figure S8c in Supporting Information S1).

This heat transport can link regional atmospheric responses over the northern IO to the Southern Ocean where the deep/bottom water forms. In climatology, strong westerly winds in the Southern Ocean drive Ekman transport equatorward, leading to a strong divergence south of 50°S at the surface and forming strong upwelling. The colder water in the deeper ocean reaches the sea surface and suppresses its warming even when the atmosphere continues to warm. This is called the MOC (also called Deacon cell; Long, Liu, et al., 2020; Morrison et al., 2016). After RF stabilization, apparent warming occurs over the Southern Ocean, which displays obvious weakening of the heat absorption above 2000 m with the MOC and atmospheric westerlies weakening (Long, Liu, et al., 2020). Because weakening upwelling leads to more heat storage over the deeper ocean and the temperature of the internal ocean becomes warmer over the upwelling zone, the ocean surface shows greater warming (Long, Liu, et al., 2020; Long, Xie, et al., 2020). This process can bring the warming signal of the deep ocean upward, and then the currents transmit energy northwards

with southwesterly currents in climatology (vectors in Figure S8a in Supporting Information S1). This is an important process associated with the regional climatic response over the northern IO with a warming signal of the deeper ocean over the Southern Ocean (Xie et al., 2010). It acts as a window contacting the warming information of the ocean with atmospheric responses.

4. Summary and Discussion

We have investigated the different patterns of rainfall change over the northern IO during RF increase and stabilization based on 13 models of CMIP5. When RF gradually increases, the rainfall increases over the tropical northern IO but decreases over the southeastern IO. The diagnose of the moisture budget reveals that the thermodynamic and dynamic components display opposite sign contributions to the rainfall response: the thermodynamic effect leads to increased (decreased) rainfall over the northern (southern) IO, while the dynamic effect contributes to a northwest-southeast dipole of rainfall change. However, after RF stabilization, the rainfall over the IO displays a totally different response, with the rainfall increasing over the southern IO but decreasing over the northern IO. A similar diagnose shows that this south-north rainfall gradient is mainly due to the effects of the atmospheric circulation response.

The anomalous vertical velocity is crucial in determining the rainfall patterns. Anomalous ascent exists where SST warming exceeds the tropical mean and leads to enhanced convective rainfall, and anomalous descent occurs where SST change is less than the tropical mean (the "warmer-get-wetter" mechanism). During RF increase, there is northwest-southeast SST asymmetry over the northern IO, the greater warming SST favors more water vapor, and anomalous ascent can transport more humidity upward over the northern IO, resulting in humidity convergence in the atmosphere, while the suppressed warming over the southeastern IO leads to anomalous descent bringing abundant humidity downward to reach the energy balance. Simultaneously, the surface easterlies transport energy to connect these ascent and descent regions. This anomalous surface wind decreases the southwesterly monsoon over the northern IO but enhances the easterly trade winds over the southern IO, which further induces changes in the SST pattern via WES feedback. The SST pattern effect is attained by adjusting the atmospheric circulation and connecting surface wind. In addition, the SST also affects the distribution of diabatic heating and stratification through homogeneous and inhomogeneous warming. The LBM outputs show that the effects of the two are partly offset, and we must consider the effects of both.

After RF stabilization, an anomalous overturning circulation occurs over the IO: it ascends over the southern IO, sinks over the northern IO and exhibits surface northerlies over the tropical IO. Similar to the situation during RF increase, this connection between SST and atmospheric circulation is well coupled to maintain this southwest-northeast SST structure. The LBM outputs show that the effects of the diabatic heating and stratification on atmospheric circulation are consistent.

Over the IO, the SST pattern is an important component of the coupled processes among atmospheric circulation, atmospheric heating and SST. To explore the formation mechanism of SST patterns, we analyzed the ocean mixed layer energy budget. After RF stabilization, ocean dynamics, especially heat transport due to temperature changes in the zonal and meridional directions, are important to display this southwest-northeast SST asymmetry. Due to the influence of deeper ocean, greater warming occurs over the southern IO, while suppressed warming resides over the northern IO. Over the Southern Ocean, the MOC slowdown leads to more heat accumulated locally and apparent warming in the deeper ocean. This dynamic circulation links the deeper ocean to the ocean surface and brings the warming signal upward. Furthermore, ocean currents transport abundant surface energy over the Southern Ocean northward to influence the IO climate. The Southern Ocean acts as a window contacting the warming signal of the deeper ocean with atmospheric circulation because there are ventilation processes to exchange matter and energy. Anomalous energy in the extratropical may cause climate change over the tropics (Kang et al., 2020).

Before we mainly focus on the total rainfall pattern over the IO, including ocean and land, but livelihood is directly impacted by rainfall over land. Through the diagnosis of the moisture budget, the patterns of rainfall change over the Indian subcontinent are mainly due to the moisture increase (thermodynamic component), but the effect of the dynamic component increases after RF stabilization (Figures 6a and 6d). The effect of ocean rainfall change is analyzed by individual apparent heat source forcing the LBM (Figures

S9 and S10 in Supporting Information S1). During RF increase, the anomalous surface southwesterlies over the northern IO are forced by the cooling over the southeastern IO and over the southern IO (Figures S9c and S9d in Supporting Information S1), which may increase water vapor transport over the Indian Peninsula. After RF stabilization, the anomalous surface northerlies over the norther IO are forced by the cooling over the northern IO (Figure S10a in Supporting Information S1), which may reduce water vapor transport over the Indian Peninsula. The influences of the other two heating are smaller (Figures S10b and S10c in Supporting Information S1). By affecting the response of atmospheric circulation, rainfall over ocean changes the water vapor transport over land, and in turn influences rainfall over land.

During RF increase, the deeper ocean accumulates heat. Its effect on the atmosphere cannot be ignored after RF stabilization, especially when the climate system is to achieve carbon neutrality. The slow response of the deeper ocean plays an important role in climate feedbacks when the carbon dioxide concentration decreases or stabilizes after the carbon neutrality (Chadwick, Wu, et al., 2013; Long et al., 2014). Our study reveals the relationship between the deeper ocean and surface atmospheric circulation, and elaborates this mechanism. Further research needs to focus on atmospheric circulation changes in greater detail. Note that, one can't ignore other potential factors for the changes of rainfall pattern over IO, like IOD (Cai et al., 2013) and Indian- Pacific relationship (Samanta et al., 2020). The different SST asymmetry pattern during RF stabilization is a special scenario that is different from the historical climate in which greater warming occurs in the Northern Hemisphere. The study of this different rainfall asymmetry patterns may provide some new findings of global warming.

Data Availability Statement

The GPCP data are available online at http://psl.noaa.gov/data/gridded/data.gpcp.html. The LBM code is available online at https://ccsr.aori.u-tokyo.ac.jp/~lbm/sub/lbm_4.html. The CMIP5 outputs are available online at https://esgf-data.dkrz.de/search/esgf-dkrz/. The related model simulations in LBM are available online at https://data.mendeley.com/datasets/hvzky7z99p/2 (https://doi.org/10.17632/hvzky7z99p.2). The mixed layer depth reanalysis data are downloaded from the Asia-Pacific Data-Research Center website (http://apdrc.soest.hawaii.edu/index.php). The radiative forcing data is from the RCP database website (https://tntcat.iiasa.ac.at/RcpDb/dsd?Action=htmlpage&page=compare).

Acknowledgments
The authors acknowledge the World Climate Research Program's Working Group on Coupled Modelling, the climate modeling groups listed in Table 1 and the U.S. Department of Energy's Program for Climate Model Diagnosis and Intercomparison for making the CMIP5 output available for present analysis. This study was supported by the National Natural Science Foundation of China (41831175), the Second Tibetan Plateau Scientific Expedition and Research (STEP) program (grant no. 2019QZKK0102), Key Deployment Project of Centre for Ocean Mega-Research of Science, the Chinese Academy of Sciences (COMS2019Q03), and the Strategic Priority Research Program of the Chinese Academy of Sciences (XDA20060501).

References

Adler, R. F., Huffman, G. J., Chang, A., Ferraro, R., Xie, P.P., Janowiak, J., et al. (2003). The version-2 global precipitation climatology project (GPCP) monthly precipitation analysis (1979-present). *Journal of Hydrometeorology*, *4*(6), 1147–1167. https://doi.org/10.1175/1525-7541(2003)004<1147:TVGPCP>2.0.CO;2

Boer, G. J., Flato, G., & Ramsden, D. (2000). A transient climate change simulation with greenhouse gas and aerosol forcing: Projected climate to the twenty-first century. *Climate Dynamics*, *16*(6), 427–450. https://doi.org/10.1007/s003820050338

Bony, S., Bellon, G., Klocke, D., Sherwood, S., Fermepin, S., & Denvil, S. (2013). Robust direct effect of carbon dioxide on tropical circulation and regional precipitation. *Nature Geoscience*, *6*, 447–451. https://doi.org/10.1038/ngeo1799

Bryan, K., Komro, F. G., Manabe, S., & Spelman, M. J. (1982). Transient climate response to increasing atmospheric carbon dioxide. *Science*, *215*(4528), 56–58. https://doi.org/10.1126/science.215.4528.56

Cai, W., Zheng, X. T., Weller, E., Collins, M., Cowan, T., Lengaigne, M., et al. (2013). Projected response of the Indian Ocean Dipole to greenhouse warming. *Nature Geoscience*, *6*(12), 999–1007. https://doi.org/10.1038/NGEO2009

Carton, J. A., Chepurin, G. A., & Chen, L. G. (2018). SODA3: A new ocean climate reanalysis. *Journal of Climate*, *31*(17), 6967–6983. https://doi.org/10.1175/JCLI-D-18-0149.1

Chadwick, R., Boutle, I., & Martin, G. (2013). Spatial patterns of precipitation change in CMIP5: Why the rich do not get richer in the tropics. *Journal of Climate*, *26*, 3803–3822. https://doi.org/10.1175/jcli-d-12-00543.1

Chadwick, R., Wu, P., Good, P., & Andrews, T. (2013). Asymmetries in tropical rainfall and circulation patterns in idealised CO_2 removal experiments. *Climate Dynamics*, *40*, 295–316. https://doi.org/10.1007/s00382-012-1287-2

Cheng, L., Abraham, J., Zhu, J., Trenberth, K. E., Fasullo, J., Boyer, T., et al. (2020). Record-setting ocean warmth continued in 2019. *Advances in Atmospheric Sciences*, *37*, 137–142. https://doi.org/10.1007/s00376-020-9283-7

Deser, C., Alexander, M. A., Xie, S. P., & Phillips, A. S. (2010). Sea surface temperature variability: Patterns and mechanisms. *Annual Review of Marine Science*, *2*, 115–143. https://doi.org/10.1146/annurev-marine-120408-151453

Dickinson, R. E. (1981). Convergence rate and stability of ocean-atmosphere coupling schemes with a zero-dimensional climate model. *Journal of the Atmospheric Sciences*, *38*, 2112–2120. https://doi.org/10.1175/1520-0469(1981)038<2112:crasoo>2.0.co;2

Richardson, T. B., Forster, P.M., Andrews, T., & Parker, D. J. (2016). Understanding the rapid precipitation response to CO2 and aerosol forcing on a regional scale. *Journal of Climate*, *29*(2), 583–594. https://doi.org/10.1175/JCLI-D-15-0174.1

Held, I. M., Winton, M., Takahashi, K., Delworth, T., Zeng, F. R., & Vallis, G. K. (2010). Probing the fast and slow components of global warming by returning abruptly to preindustrial forcing. *Journal of Climate*, *23*(9), 2418–2427. https://doi.org/10.1175/2009JCLI3466.1

Hoffert, M. I., Callegari, A. J., & Hsieh, C.-T. (1980). The role of deep sea heat storage in the secular response to climatic forcing. *Journal of Geophysical Research*, *85*(C11), 6667–6679. https://doi.org/10.1029/JC085iC11p06667

Hwang, Y. T., Xie, S. P., Deser, C., & Kang, S. M. (2017). Connecting tropical climate change with Southern Ocean heat uptake. *Geophysical Research Letters*, *44*, 9449–9457. https://doi.org/10.1002/2017GL074972

IPCC. (2018). Summary for Policymakers. In V. Masson-Delmotte, P. Zhai, H.-O. Pörtner, D. Roberts, J. Skea, & P. R. Shukla, et al. (Eds.), *Global warming of 1.5°C. An IPCC Special Report on the impacts of global warming of 1.5°C above pre-industrial levels and related global greenhouse gas emission pathways, in the context of strengthening the global response to the threat of climate change, sustainable development, and efforts to eradicate poverty* (pp. 32). World Meteorological Organization.

Kang, S. M., Xie, S.-P., Shin, Y., Kim, H., Hwang, Y. T., Stuecker, M. F., et al. (2020). Walker circulation response to extratropical radiative forcing. *Science Advances*, *6*(47), eabd3021. https://doi.org/10.1126/sciadv.abd3021

Knutson, T. R., & Manabe, S. (1995). Time-mean response over the Tropical Pacific to increased CO2 in a coupled ocean-atmosphere model. *Journal of Climate*, *8*(9), 2181–2199. https://doi.org/10.1175/1520-0442(1995)008<2181:TMROTT>2.0.CO;2

Long, S. M., Liu, Q., Zheng, X. T., Cheng, X. H., Bai, X. Z., & Gao, Z. (2020). Research progress of long-term ocean temperature changes in the Southern Ocean. *Advance in Earth Sciences*, *35*(9), 962–977. https://doi.org/1001-8166(2020)35:9<962:NDYHWC>2.0.TX;2-F

Long, S. M., Xie, S. P., Du, Y., Liu, Q. Y., Zheng, X. T., Huang, G., et al. (2020). Effects of ocean slow response under low warming targets. *Journal of Climate*, *33*(2), 477–496. https://doi.org/10.1175/JCLI-D-19-0213.1

Long, S. -M., Xie, S. -P., Liu, Q., Zheng, X. -T., Huang, G., Hu, K., & Du, Y. (2018). Slow ocean response and the 1.5 and 2°C warming targets. *Chinese Science Bulletin*, *63*, 558–570. https://doi.org/10.1360/n972017-01115

Long, S. M., Xie, S. P., Zheng, X. T., & Liu, Q. Y. (2014). Fast and slow response to global warming: Sea surface temperature and precipitation patterns. *Journal of Climate*, *27*(1), 285–299. https://doi.org/10.1175/JCLI-D-13-00297.1

Ma, J., Chadwick, R., Seo, K. H., Dong, C., Huang, G., Foltz, G. R., & Jiang, J. H. (2018). Responses of the tropical atmospheric circulation to climate change and connection to the hydrological cycle. *Annual Review of Earth and Planetary Sciences*, *46*, 549–580. https://doi.org/10.1146/annurev-earth-082517-010102

Ma, J., & Xie, S. P. (2013). Regional patterns of sea surface temperature change: A source of uncertainty in future projections of precipitation and atmospheric circulation. *Journal of Climate*, *26*(8), 2482–2501. https://doi.org/10.1175/JCLI-D-12-00283.1

Ma, J., Xie, S. P., & Kosaka, Y. (2012). Mechanisms for tropical tropospheric circulation change in response to global warming. *Journal of Climate*, *25*(8), 2979–2994. https://doi.org/10.1175/JCLI-D-11-00048.1

Manabe, S., Bryan, K., & Spelman, M. J. (1990). Transient response of a global ocean-atmosphere model to a doubling of atmospheric carbon dioxide. *Journal of Physical Oceanography*, *20*(5), 722–749. https://doi.org/10.1175/1520-0485(1990)020<0722:TROAGO>2.0.CO;2

Manabe, S., & Stouffer, R. J. (2007). Role of ocean in global warming. *Journal of the Meteorological Society of Japan*, *85B*, 385–403. https://doi.org/10.2151/jmsj.85B.385

Morrison, A. K., Griffies, S. M., Winton, M., Anderson, W. G., & Sarmiento, J. L. (2016). Mechanisms of Southern Ocean heat uptake and transport in a global eddying climate model. *Journal of Climate*, *29*(6), 2059–2075. https://doi.org/10.1175/JCLI-D-15-0579.1

Ng, B., Cai, W.-J., Walsh, K., & Santodo, A. (2015). Nonlinear processes reinforce extreme Indian Ocean Dipole events. *Science Reports*, *5*, 11697. https://doi.org/10.1038/srep11697

Qu, X., Huang, G., Hu, K. M., Xie, S. P., Du, Y., Zheng, X. T., & Liu, L. (2015). Equatorward shift of the South Asian high in response to anthropogenic forcing. *Theoretical and Applied Climatology*, *119*(1-2), 113–122. https://doi.org/10.1007/s00704-014-1095-1

Richter, I., & Xie, S.-P. (2008). Muted precipitation increase in global warming simulations: A surface evaporation perspective. *Journal of Geophysical Research*, *113*(4). https://doi.org/10.1029/2008JD010561

Samanta, D., Rajagopalan, B., Karnauskas, K. B., Zhang, L., & Goodkin, N. F. (2020). La Niña's diminishing fingerprint on the central Indian summer monsoon. *Geophysical Research Letters*, *47*(2), e2019GL08623. https://doi.org/10.1029/2019GL086237

Sanderson, B. M., O'Neill, B. C., & Tebaldi, C. (2016). What would it take to achieve the Paris temperature targets? *Geophysical Research Letters*, *43*, 7133–7142. https://doi.org/10.1002/2016GL069563

Seager, R., Naik, N., & Vecchi, G. A. (2010). Thermodynamic and dynamic mechanisms for large-scale changes in the hydrological cycle in response to global warming. *Journal of Climate*, *23*, 4651–4668. https://doi.org/10.1175/2010jcli3655.1

Seth, A., Giannini, A., Rojas, M., Rauscher, S. A., Bordoni, S., Singh, D., & Camargo, S. J. (2019). Monsoon responses to climate changes-Connecting past, present and future. *Current Climate Change Reports*, *5*(2), 63–79. https://doi.org/10.1007/s40641-019-00125-y

Sniderman, J. M. K., Brown, J. R., Woodhead, J. D., King, A. D., Gillett, N. P., Tokarska, K. B., et al. (2019). Southern hemisphere subtropical drying as a transient response to warming. *Nature Climate Change*, *9*, 232–236. https://doi.org/10.1038/s41558-019-0397-9

Stouffer, R. J. (2004). Time scales of climate response. *Journal of Climate*, *17*, 209–217. https://doi.org/10.1175/1520-0442(2004)017<0209:tsocr>2.0.co;2

Vecchi, G. A., & Soden, B. J. (2007). Global warming and the weakening of the tropical circulation. *Journal of Climate*, *20*, 4316–4340. https://doi.org/10.1175/jcli4258.1

von Schuckmann, K., Palmer, M. D., Trenberth, K. E., Cazenave, A., Chambers, D., Champollion, N., et al. (2016). An imperative to monitor Earth's energy imbalance. *Nature Climate Change*, *6*(2), 138–144. https://doi.org/10.1038/NCLIMATE2876

Wang, B., Jin, C. H., & Liu, J. (2020). Understanding future change of global monsoons projected by CMIP6 models. *Journal of Climate*, *33*(15), 6471–6489. https://doi.org/10.1175/JCLI-D-19-0993.1

Wang, B., Yim, S. Y., Lee, J. Y., Liu, J., & Ha, K. J. (2014). Future change of Asian-Australian monsoon under RCP 4.5 anthropogenic warming scenario. *Climate Dynamics*, *42*(1–2), 83–100. https://doi.org/10.1007/s00382-013-1769-x

Watanabe, M., & Kimoto, M. (2000). Atmosphere-ocean thermal coupling in the North Atlantic: A positive feedback. *Quarterly Journal of the Royal Meteorological Society*, *126*, 3343–3369. https://doi.org/10.1002/qj.49712657017

Xie, S.P., Deser, C., Vecchi, G. A., Ma, J., Teng, H.Y., & Wittenberg, A. T. (2010). Global warming pattern formation: Sea surface temperature and rainfall. *Journal of Climate*, *23*(4), 966–986. https://doi.org/10.1175/2009JCLI3329.1

Yanai, M., Esbensen, S., & Chu, J. H. (1973). Determination of bulk properties of tropical cloud clusters from large-scale heat and moisture budgets. *Journal of the Atmospheric Sciences*, *30*, 611–627. https://doi.org/10.1175/1520-0469(1973)030<0611:dobpot>2.0.co;2

Ying, J., Huang, P., & Huang, R.H. (2016). Evaluating the formation mechanisms of the equatorial Pacific SST warming pattern in CMIP5 models. *Advances in Atmospheric Sciences*, *33*(4), 433–441. https://doi.org/10.1007/s00376-015-5184-6

Reference From the Supporting Information

DiNezio, P. N., Clement, A. C., Vecchi, G. A., Soden, B. J., Kirtman, B. P., & Lee, S. K. (2009). Climate response of the equatorial pacific to global warming. *Journal of Climate*, *22*, 4873–4892. https://doi.org/10.1175/2009jcli2982.1